A multi-objective optimization-based layer-by-layer blade-coating approach for organic solar cells

Sun, Rui; Guo, Jie; Wu, Qiang; Zhang, Zhuohan; Yang, Wenyan; Guo, Jing; Shi, Mumin; Zhang, Yaohong; Kahmann, Simon; Ye, Long

Published in:
Energy & Environmental Science

DOI:
10.1039/c9ee02295c

Energy & Environmental Science

PAPER

View Article Online
View Journal | View Issue

Cite this: *Energy Environ. Sci.*, 2019, **12**, 3118

A multi-objective optimization-based layer-by-layer blade-coating approach for organic solar cells: rational control of vertical stratification for high performance†

Rui Sun,[a] Jie Guo,[a] Qiang Wu,[a] Zhuohan Zhang,[b] Wenyan Yang,[a] Jing Guo,[a] Mumin Shi,[a] Yaohong Zhang,[c] Simon Kahmann,[d] Long Ye,[e] Xuechen Jiao,[f] Maria A. Loi,[d] Qing Shen,[c] Harald Ade,[e] Weihua Tang,[b] Christoph J. Brabec[g] and Jie Min*[a]

A major breakthrough in organic solar cells (OSCs) in the last thirty years was the development of the bulk heterojunction (BHJ) solution processing strategy, which effectively provided a nanoscale phase-separated morphology, aiding in the separation of Coulombically bound excitons and facilitating charge transport and extraction. Compared with the application of the layer-by-layer (LbL) approach proposed in the same period, the BHJ spin-coating technology shows overwhelming advantages for evaluating the performance of photovoltaic materials and achieving more-efficient photoelectric conversion. Thus, in this study, we have further compared the BHJ and LbL processing strategies *via* the doctor-blade coating technology because it is a roll-to-roll compatible high-throughput thin film fabrication route. We systematically evaluated multiple target parameters, including morphological characteristics, optical simulation, physical kinetics, device efficiency, and blend stability issues. It is worth emphasizing that our findings disprove the old stereotypes such as the BHJ processing method is superior to the LbL technology for the preparation of high-performance OSCs and the LbL approach requires an orthogonal solvent and donor/acceptor materials with special solubility. Our studies demonstrate that the LbL blade-coating approach is a promising strategy to effectively reduce the efficiency-stability gap of OSCs and even a superior alternative to the BHJ method in commercial applications.

Received 19th July 2019,
Accepted 21st August 2019

DOI: 10.1039/c9ee02295c

rsc.li/ees

Broader context

The photovoltaic performance, including device efficiency and stability, of solution-processed organic solar cells (OSCs) is strongly correlated to the bulk heterojunction (BHJ) blend microstructure of specific photoactive materials or systems. In recent decades, the BHJ solution processing approach has taken an irreplaceable lead in the development of OSCs and recently pushed the PCEs to a record high value. However, it still has some drawbacks. Thus, finding effective and highly repeatable ways to control the morphology is still one of the most important research subjects in the OSC field. Based on this, we diverted our interest to building optimal morphologies with the p–i–n architecture *via* the layer-by-layer (LbL) blade-coating technique, which was economical and easily transferable to a roll-to-roll (R2R) coating environment. In this contribution, we minutely depicted the intrinsic characteristics of BHJ and LbL blends during the film formation, and systematically evaluated their multiple target parameters, including morphological characteristics, optical simulation, physical kinetics, device efficiency, and blend stability issues. The results highlight that the LbL approach is more beneficial to reduce the efficiency-stability gap of OSCs and even a superior alternative to the BHJ method in commercial applications.

[a] *The Institute for Advanced Studies, Wuhan University, Wuhan 430072, China. E-mail: min.jie@whu.edu.cn*
[b] *Key Laboratory of Soft Chemistry and Functional Materials, Ministry of Education, Nanjing University of Science and Technology, Nanjing 210094, China*
[c] *Faculty of Informatics and Engineering, The University of Electro-Communications, 1-5-1 Chofugaoka, Tokyo 182-8585, Japan*
[d] *Zernike Institute for Advanced Materials, University of Groningen, NL-9747AG, Groningen, The Netherlands*
[e] *Department of Physics and Organic and Carbon Electronics Laboratory (ORaCEL), North Carolina State University, Raleigh, NC 27695, USA*
[f] *Department of Materials Science and Engineering, Monash University, Victoria, Australia*
[g] *Institute of Materials for Electronics and Energy Technology (i-MEET), Department of Materials Science and Engineering, Friedrich-Alexander-Universität Erlangen-Nürnberg, Martensstr. 7, 91058 Erlangen, Germany*

† Electronic supplementary information (ESI) available. See DOI: 10.1039/c9ee02295c

1. Introduction

The photovoltaic performance of solution-processed organic solar cells (OSCs) is strongly correlated to the blend microstructure of specific photoactive materials or systems.[1–5] The strategies developed for morphology control in the past three decades can be divided into three categories, as depicted in Fig. 1a: vacuum evaporated planar bilayer structure strategy, solution-processed bulk heterojunction (BHJ) structure strategy, and layer-by-layer (LbL, or pseudo-bilayer) structure strategy. In the middle of the 1980s, the vacuum evaporated donor/acceptor (D/A) bilayer heterojunction architecture was intensively investigated.[6] However, devices with this architecture typically have a very low power conversion efficiency (PCE) of approximately 1% due to the short exciton diffusion length in organic materials (typically 5–20 nm).[7,8] Thus, to overcome the drawbacks of this type of active layer structure, as early as 1995, Heeger *et al.* created the BHJ concept and fabricated a nanoscale phase-separated morphology with a larger D/A interface area.[9] Benefiting from its suitable microstructure for the separation of bound singlet excitons into free charge pairs, the BHJ processing technology significantly enhances the short-circuit current density (J_{sc}) and thus improves the device efficiency.[2,10–12] Subsequently, the BHJ approach has taken an irreplaceable lead in the development of OSCs and recently pushed the PCEs to a record high value.[13–18]

However, the BHJ structure, which is viewed as a mixture of donor-rich, acceptor-rich and mixed amorphous or disordered D/A domains resulting from the partial miscibility of the components, still has some insurmountable disadvantages. First, optimization of the BHJ morphology, including its crystallinity, molecular order and orientation, domain size and purity, and distribution of its components, is highly sensitive to the material properties, processing conditions, surrounding environment and post-treatments.[5,19–22] Second, the optimal morphologies of the BHJ structure can allow efficient exciton dissociation and balanced charge transport properties, but they are usually in a metastable state and will further move toward a thermodynamic equilibrium state, resulting in phase separation, mainly accelerated by the inherently low miscibility of D/A materials[23] or accumulated heat.[24–26] Based on this view, the growing understanding of the use of processes to control and tune morphology through chemical or processing methods is allowing rapid progress to be made in the development of high-performance BHJ OSCs. Numerous strategies, including the addition of cross-linkable groups and volatilizable solid additives,[26,27] introduction of molecular locking strategy,[28] development of alloy components,[29,30] and modification of material structure and photoactive systems,[25,31–33] have been demonstrated to be able to modify and solidify the BHJ morphology. Nevertheless, these processing approaches are generally limited by individual photovoltaic systems and are still not the best option. Thus, finding effective and highly repeatable ways to control the morphology is still one of the most important research subjects in the OSC field, which is a challenging task.

One widely held view is that an optimal active layer morphology should be a pseudo-bilayer configuration (such as a p–i–n (D/D : A/A) structure, Fig. 1a).[34–36] Thus, many strategies, including nanoimprint lithography,[37] LbL vacuum deposition or solution process,[36,38] and stamping or lamination methods,[39] have been developed to effectively form the pseudo-bilayer configuration. Among them, the LbL solution processing approach is an unavoidable option to construct the optimal morphology of the active layer. In 2009, Ayzner *et al.* first reported the strategy of sequentially and separately depositing the electron donor poly(3-hexylthiophene-2,5-diyl) (P3HT) and acceptor [6,6]-phenyl-C61-butyric acid methyl ester (PCBM) from orthogonal solvents.[40] Subsequently, several other groups reported that by using this LbL approach, similar or even better PCEs compared with that of BHJ devices were obtained for many photovoltaic fullerene and non-fullerene systems.[35,41–44] However, these LbL blends were formed by sequential spin-coating from solutions of orthogonal solvents, which do not appear to be suitable for the large-scale fabrication of OSCs. In our previous work, inspired by the results from spin-coating and its inherent defects,[36] we diverted our interest to building the optimal morphology *via* the LbL blade-coating technique (Fig. 1b). The doctor-blade (DB) coating technology is inexpensive and easily transferable to a roll-to-roll (R2R) coating environment. However, to date, the few well demonstrated studies have reported on the sequentially bladed LbL structure and mainly focused on device efficiency comparisons.[36,43] To quickly drive OSCs from the laboratory to industry,[13] the BHJ and LbL approaches should be systematically investigated and compared, and then selected for commercial applications. Thus, further gaining in-depth knowledge and comprehensive evaluation of the LbL-bladed architecture are essential and urgent, especially when the device efficiency is approaching the theoretical value.[45]

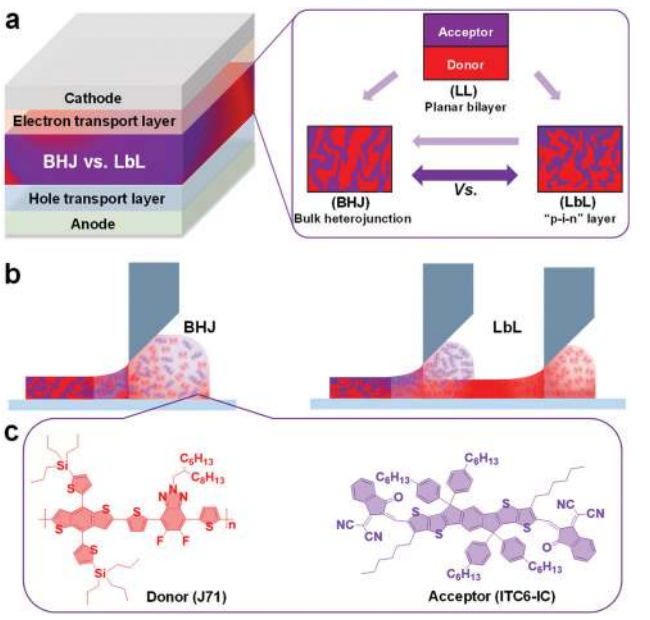

Fig. 1 (a) Schematic device architecture of OSCs and the common active layer configurations, (b) schematic of the BHJ and LbL blade-coating approaches and (c) chemical structures of the donor and acceptor materials investigated in this work.

Herein, we focused our endeavor to depict in detail the intrinsic characteristics of BHJ and LbL blends. The subject of this study is the polymer donor J71[46] blended with ITC6-IC as the acceptor,[47] as shown in Fig. 1c. In detail, we firstly applied an *in situ* photoluminescence (PL) setup to delineate the nanoscale microstructure evolution of active layers processed either by the BHJ or LbL approach and also subjected to long-time thermal annealing (TA) treatment. Thus, the different dynamic effects of the BHJ and LbL approaches on morphology evolution during the film preparation and heat treatment and the influence of morphological characteristics on device degradation processes are analyzed. In addition, the optical spectrum and simulations were investigated to compare the absorption coefficient of the BHJ and LbL blends and their photo-absorption rate in the investigated devices. Based on this analysis, we further determined the correlation between the measured characteristics of the blend morphologies and the explored the mechanisms for the photo-induced charge generation in devices. Importantly, the correlations between morphological characteristics, optical simulation, physical kinetics, and device performance in the J71:ITC6-IC system were explored. Furthermore, a thorough discussion on the direct correlations between the relevant blends and their device performance is provided to highlight that the LbL approach is more beneficial to reduce the efficiency-stability gap of OSCs compared to the BHJ method.

2. Results

2.1. Description of device fabrication and device performance

The device architecture and film-forming techniques (BHJ and LbL *via* doctor-bladed coating process) used in this study are shown in Fig. 1a and b, respectively. Details of the BHJ and LbL processing approaches are described in the Experimental section in the ESI.† The absorption spectra of the pristine J71 and ITC6-IC films are provided in Fig. S1 (ESI†). The photovoltaic performance of the corresponding OSCs based on bladed BHJ and LbL active layers and their external quantum efficiency (EQE) curves are shown in Fig. S2 in the ESI† and the relevant parameters are summarized in Table S1 (ESI†). The OSCs based on the J71:ITC6-IC LbL blend show comparable PCEs with our previous reported results, which are higher than that of BHJ-based devices.[36] Of note is that our current work is an in-depth analysis and discussion into the specific advantages of the LbL doctor-blading approach with the exception of device efficiency comparisons.

As is known, unlike the BHJ processing method, which requires the preparation of a D : A mixed solution and screening relevant D : A weight ratios, the LbL strategy generally has an extra step, which involves the deposition of the relevant acceptor layer on the donor film. Thus, further distinctions associated with the effects of the BHJ and LbL approaches on the formation, optimization, and degradation of the blend morphology should be determined, which is investigated in the following section.

2.2. *In situ* morphology evolution of BHJ and LbL blends

The real-time evolution of the BHJ and LbL blend morphologies coated by the doctor-blade technique was investigated *via in situ* photoluminescence (PL) spectroscopy. A doctor-blade coater was mounted in a fume hood in an air atmosphere, where the blade was translated over the substrate with the PL probe incident on the sample at a fixed distance from the blade, as shown in Fig. S3 (ESI†). This not only enabled the *in situ* characterization of the morphology as the solvent was evaporating but also monitoring the morphology evolution during the TA treatment. In this section, emphasis is placed on the multimodal studies combining sensitive *in situ* PL with relevant optical and morphological characterizations for clearly defining the evolution of the solute structure, including aggregation, crystallinity, topography, domain size, phase separation, and vertical component distribution. As a result, a clear schematic presentation of the BHJ and LbL morphology characteristics based on the J71:ITC6-IC system is given.

2.2.1. Film formation of BHJ and LbL layers. Fig. 2a and b show the *in situ* PL results, where it is evident that both phase separation and material ordering occurred much more rapidly with a decrease in chloroform (CF) concentration. The PL intensities of the BHJ and LbL processes gradually reduced from 0 s to 11.5 s. During the J71:ITC6-IC BHJ film formation, the rapid removal of CF due to the heating of the substrate very rapidly concentrated the J71:ITC6-IC mixture well past the solubility limit, driving the wetting deposition to layer-thinning transition. The different limit of saturation of donor and acceptor materials in the mixed solvent and their special surface energy and miscibility influence the growth and connectivity of the aggregates formed. As exhibited in Fig. 2c, the position of the PL peak gradually shifted from 753 nm to 756 nm after 7 s of blade coating, indicating that the J71:ITC6-IC BHJ mixture forced a phase separation before a primary crystallization of ITC6-IC. Unlike the BHJ process, the position of the PL peak remained unchanged during the removal of CF in the LbL mixture. Note that these PL signals during the LbL film formation were monitored by scraping the acceptor solution onto the donor thin film. In addition, unlike the BHJ film formation with the height of the PL peak reduced by one-fifth of the original PL signal, that of LbL film formation was only reduced by half. Combined with the higher peak position of the LbL mixture in the J71/ITC6-IC LbL film formation (Fig. 2c) and the PL spectra of the D/A pristine films (Fig. S4, ESI†), we can conclude that the deposition of the upper acceptor ITC6-IC did not completely dissolve the J71 thin film.

2.2.2. Thermal annealing treatments of BHJ and LbL layers. As discussed above, both the BHJ and LbL blends needed to undergo TA treatments for 5 minutes at 150 °C for further modifying the blend microstructure, thus resulting in high PCEs in both devices. As shown in Fig. 2e and f, detailed characterization of the evolution of the blend morphology during the TA treatment from the sub-nanometer to tens of nanometers could also be achieved using the PL signal. Interestingly, the peak position of the BHJ film gradually decreased in the first minute, then increased in the next two minutes, and stabilized after three minutes, as depicted in Fig. 2g. Meanwhile, the peak height for the BHJ film gradually increased in the first two minutes, then decreased in the next two minutes, and stabilized after four minutes. Thus, the

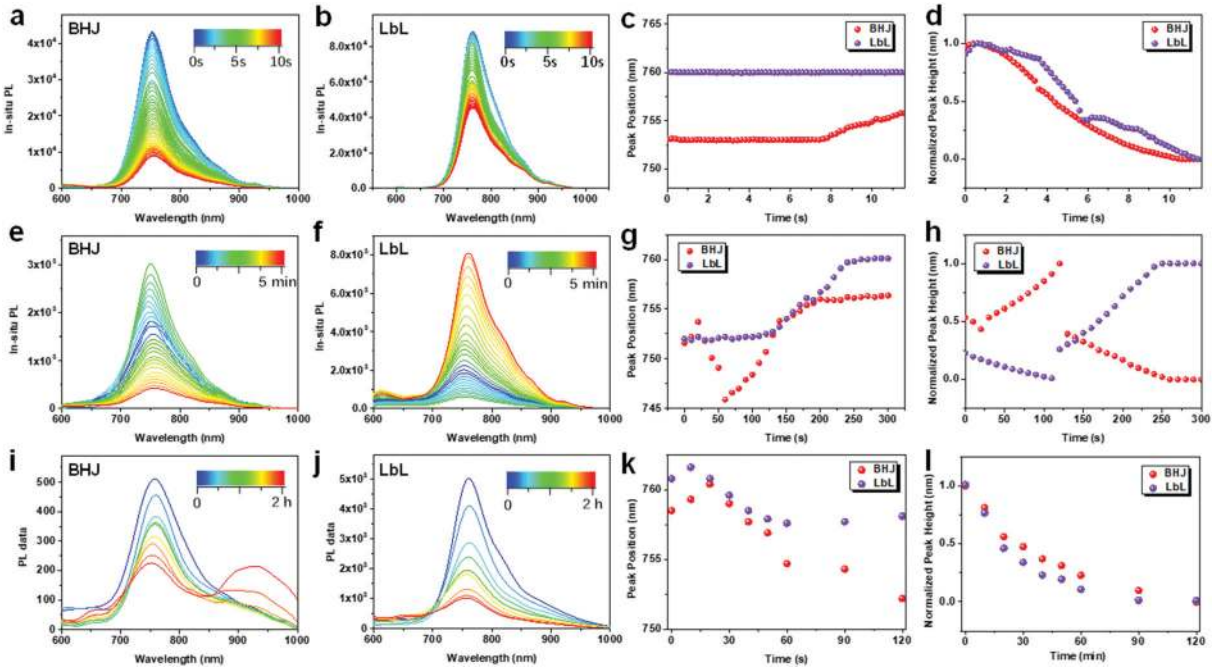

Fig. 2 Evolution of *in situ* PL during the (a) BHJ and (b) LbL layer formation processes, and the corresponding (c) peak position and (d) normalized peak height plotted from 0 s to 11.5 s. PL evolution of the (e) BHJ and (f) LbL layers during thermal annealing treatment at a temperature of 150 °C, and the corresponding (g) peak position and (h) normalized peak height plotted from 0 min to 5 min. PL spectra changes of the (i) BHJ and (j) LbL layers during heat aging treatments at a temperature of 150 °C, and the corresponding (k) peak position and (l) normalized peak height plotted from 0 to 2 h.

changes in the PL spectra during the TA treatment of the BHJ film illustrate two morphological evolution processes, where the former is the increasing phase separation of the BHJ blend, and the latter is mainly due to the secondary crystallization of the acceptor materials. In contrast to the BHJ blend subjected to TA treatment, the peak position of the LbL thin film gradually increased from 752 nm to 760 nm within the first four minutes, and then remained stable afterwards. In addition, the peak height of the LbL film gradually decreased in the first two minutes, and then increased in the next two minutes. Combined with the morphological characteristics of the LbL film formation, the changes in the morphology evolution during the TA treatment of LbL film also indicates two main processes, including secondary crystallization of the acceptor materials and their crystal growth after two minutes of TA treatment. Thus, the morphologies of the BHJ and LbL blends during the TA treatments have different evolutions, which further illustrate the differences between these two optimal microstructures.

2.2.3. Thermal stability of the BHJ and LbL morphologies. The above-discussed results drove us to understand the thermal stability of the BHJ and LbL morphologies. Here, we further heated the two types of films to a high temperature of 150 °C and measured the evolution of their PL signals, as presented in Fig. 2i and j. Note that these samples were heated in a glovebox in the dark to avoid photo-oxidation issues.[45] The peak heights of both the BHJ and LbL films gradually decreased as shown in Fig. 2l, which is probably due to the further crystallization of the D and A materials in their blends. However, distinctly different behaviors for the peak position based on these two blends can be observed in Fig. 2k. After 1 h heat treatment, the peak position of the BHJ film still decreased continuously, whereas the peak position of the LbL film still remained stable. It should be noted that additional near-infrared peaks appeared in the PL spectra of the aged BHJ film after 1 h heating (Fig. 2i), while its peak height gradually increased with heating time. These results indicate the strong crystallization of the acceptor materials and obvious trend of secondary phase separation in the heated BHJ film. Thus, a preliminary conclusion can be drawn that the LbL blend is more stable under heat than the formed BHJ blend. A more detailed description and analysis of the thermal stability of the relevant blends will be provided in the Discussion section.

2.3. Microstructures of the optimal BHJ and LbL blends

From our *in situ* PL measurements, we found that the film formation and optimization of the BHJ active layer, as well as its thermal degradation, are not identical to the corresponding processes of the LbL blend. Thus, in the following sections, we characterize both the lateral and vertical domain morphologies, as well as the molecular packing and crystallinity across the BHJ and LbL active layers.

2.3.1. Lateral Morphology. The optimal morphologies of the BHJ and LbL blends were first investigated by atomic force microscopy (AFM) and transmission electron microscopy (TEM) measurements. Fig. 3a and b show the AFM surface images of the optimal BHJ and LbL blends. Note that the films were prepared under the same conditions that the related devices were fabricated. The AFM image of the BHJ blend exhibits very smooth surfaces with no visible macroscopic phase separation.

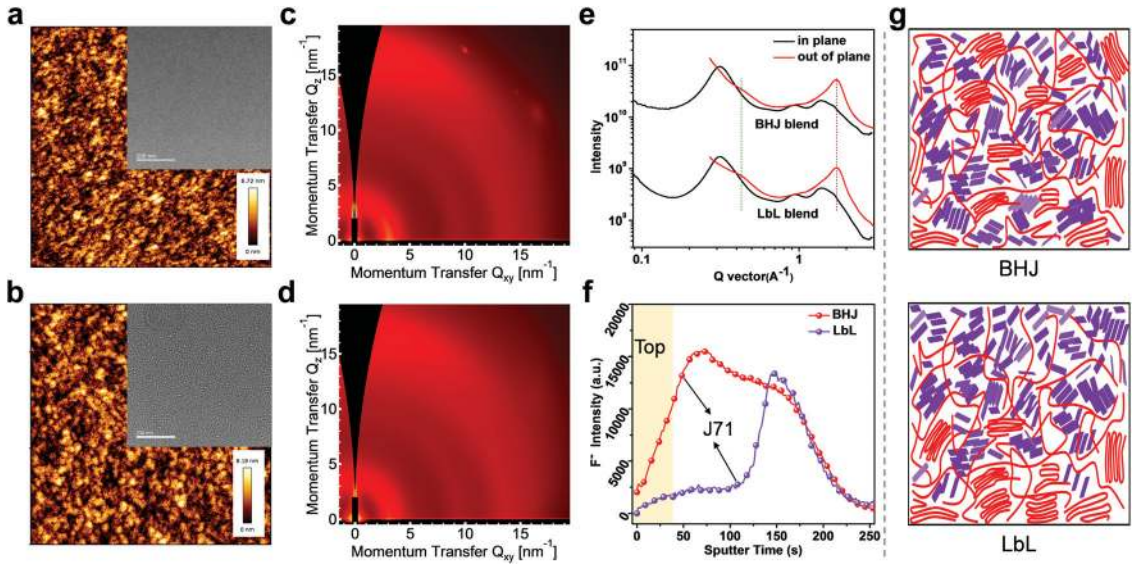

Fig. 3 Surface topographic and phase AFM images (size: 5 × 5 μm^2) of (a) J71:ITC6-IC BHJ (root mean square (RMS) = 1.5 nm; inset: TEM image) and (b) J71/ITC6-IC LbL (RMS = 1.2 nm; inset: TEM image) films. GIWAXS scattering results of (c) BHJ and (d) LbL blends with TA treatments. All images were corrected for monitor and film thickness and displayed on the same logarithmic color scale. (e) In-plane (IP) and out-of-plane (OOP) profiles of the BHJ and LbL films acquired at the critical incident angle of 0.13°. (f) TOF-SIMS ion yield as a function of sputtering time for the BHJ and LbL samples. The depth profile of the J71 polymer by tracing F^- is shown. (g) Schematic representation of the morphological characteristics of the BHJ and LbL blends.

However, this amorphous morphology at the nanoscale lacks percolated pathways to the electrodes, and thus suffers from increased carrier recombination.[49] In contrast, the phase separation of the LbL blend with a clearer bi-continuous network is observed over its entire surface. These networks can act as "highways" for efficient exciton diffusion and charge extraction, and thus contribute to the enhanced device performance.[21] Both the BHJ and LbL blends show small root-mean-square (RMS) surface roughness (1.5 nm for BHJ and 1.2 nm for LbL). More insight into the bulk microstructure was obtained from the TEM investigations (Fig. 3a and b, insets), which show uniform surfaces for the BHJ film without any significant crystallization or phase separation. In contrast, in the LbL film, nanoscale phase separation was obvious.

2.3.2. Crystallinity. The π–π stacking peak for the pristine J71 film is preferentially oriented in the out-of-plane direction (Fig. S5a, ESI†). In contrast, that for the pristine ITC6-IC film is highly disordered (Fig. S5b, ESI†), with weak diffusive scattering from lamellar packing. As shown in Fig. 3c and d, a strong out-of-plane scattering peak was observed for the BHJ and LbL films treated by TA. Notably, the 2D GIWAXS measurements did not reveal distinctly different scattering patterns for the blends bladed by the BHJ and LbL approaches. These results are different from that in previous investigations on spin-coated BHJ and LbL films.[36] Both the BHJ and LbL films showed diffusive out-of-plane scattering around 1.8 Å^{-1}, as shown in Fig. 3e. In addition, we further performed angle-dependent GIWAXS measurements (Fig. S5c and d, ESI†). The shallow incidence angle of 0.02° was chosen to investigate the crystallization close to the top surface of the films. The GIWAXS results for the BHJ blend did not show any in-plane lamellar stacking diffraction peaks (Fig. S5e, ESI†). In contrast, the LbL blend revealed the presence of ITC6-IC crystallites in the upper part of its active layer, as evidenced by the corresponding diffraction (Fig. S5f, ESI†). Thus, this observation unambiguously proves the existence of ordered ITC6-IC top layers in the LbL layers.

2.3.3. Vertical composition profiles. The GIWAXS profiles of both blends acquired at the critical angle of 0.02° only provide insight into the crystallinity of their surface morphology, and thus are not necessarily representative for the vertical composition profiles of the thin films. Therefore, to gain insight into the internal structure and vertical phase characteristics of the BHJ and LbL blends, we further conducted time-of-flight secondary ion mass spectrometry (TOF-SIMS) measurements, which quantitatively monitored the vertical profiles of each component across the whole thickness of the active layers.[5] As shown in Fig. 3f, we observed the characteristic mass fragments of the BHJ and LbL blends. Note that fluorine (F) was used to track the J71 polymer donor. An escalating F signal was obtained at the beginning of the sputtering, which indicated a donor-rich surface in the BHJ blend coated by the mixed solution. In contrast to the BHJ processing method, in the LbL coating process, the J71 layer was coated firstly and then the ITC6-IC layer was deposited on it. Combined with the F signal depicted in Fig. 3f, we can easily conclude that the ITC6-IC acceptors were assembled at the LbL/air surface, and the J71 donors were enriched at the bottom of the LbL blend. Again, this suggests distinctly different film formation characteristics for the BHJ and LbL technologies, and dynamic patterns for the corresponding BHJ and LbL morphologies.

Here, our in-depth morphological analyses provide a detailed description of the aggregation patterns and vertical phase separation in the optimal BHJ and LbL blends, as depicted in Fig. 3g. By combining all the findings from these morphological

characterizations, we conclude that the LbL coating process can effectively modify the vertical phase components.[36] In contrast, although the BHJ coating process can achieve nanoscale phase separation, it leaves the BHJ blend relatively disordered in the vertical phase. Undoubtedly, the distinct 3D microstructures of the BHJ and LbL blends are also reflected in their optical absorption profiles, which were investigated in the next section.

2.4. Optical simulations of BHJ and LbL systems

Compared to the optimal BHJ blend, as shown in Fig. 4a, the optimal LbL blend showed a slightly red-shifted absorption spectrum with a higher absorption coefficient of approximately 8.0×10^4 cm^{-1}, indicating enhanced molecular ordering of the ITC6-IC acceptors demonstrated by the above-mentioned morphology characterizations. The higher absorption coefficient suggests that a greater number of photons in the LbL blend can be absorbed and converted into energy, which was demonstrated by the measurement of the photovoltaic parameters (Fig. S2, ESI†). Here, we simulated the maximum J_{sc} values and photo-absorption rate in the devices to further highlight the advantage of the LbL blade-processing strategy.

2.4.1. Simulated maximum J_{sc} values. The difference in optical absorption drove us to employ spectroscopic ellipsometry to determine the accurate optical constants (n and k) for the BHJ and LbL layers, as shown in Fig. 4b. It should be noted that our ellipsometric n and k analysis used films with different thicknesses (Fig. S6, ESI†) to avoid any issues with morphology-induced thickness dependence of the optical constants.[50] Moreover, exceptional care was taken in measuring the extinction coefficients and thicknesses of the active layer materials in order to make the photocurrent estimates as accurate as possible. As depicted in Fig. 3g, when the films were fabricated *via* the LbL blading method, fast molecular aggregation of ITC6-IC was observed before it dropped down to the J71 bottom region. This benefits the already formed crystallites and enhances the absorption coefficient of the active layer, as demonstrated by the ellipsometric n and k analysis. As shown in Fig. 4b, both the BHJ and LbL films exhibit quite marked differences. Fig. 4c shows the plot of simulated photocurrent assuming 100% internal quantum efficiency (IQE, and weighted by the AM1.5G solar spectrum) as a function of cavity thickness. For comparison, the actual J_{sc} values were measured in several cells with different active layer thicknesses in the BHJ and LbL devices. The effects of thickness on the J–V curve characteristics of the BHJ and LbL devices are exhibited in Fig. S7 (ESI†) and the relevant photovoltaic parameters are summarized in Table S2 (ESI†). Also, the plots of simulated current density (J_{opt}) and observed J_{sc} values *versus* film thickness are shown in Fig. 4c. Both the BHJ and LbL blends exhibit peak efficiencies with thin active layers near the first interference maximum (80–100 nm). As the thickness increases from approximately 125 nm, it was found that the predicted maximum photocurrent of the LbL system became smoother than that of the BHJ system with a wave rising trend feature. Besides, since increased recombination substantially reduces the IQE, while real devices have less than 100% IQE,[50,51] the simulated and measured photocurrents slightly diverge in thicker active layers. These trends are consistent with the FF values of the BHJ and LbL devices when their thicknesses are beyond 125 nm

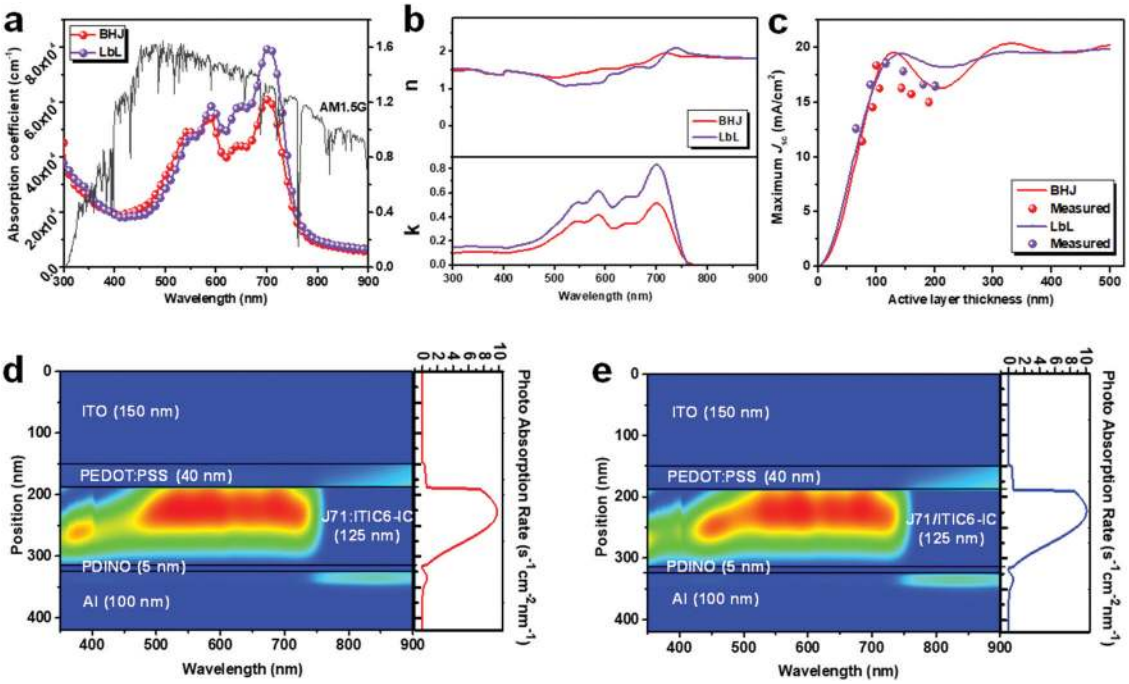

Fig. 4 (a) Optical properties of the optimal BHJ and LbL active layers. (b) Optical constants (n and k) of the involved active layers. (c) Simulated maximum J_{sc} with an increase in the photoactive layer thickness. Simulated photoabsorption rate in the J71:ITC6-IC-based OSCs with active layer thicknesses of 125 nm using the (d) BHJ and (e) LbL architectures.

(Table S2, ESI†). Nevertheless, the measured photocurrents of the devices based on thicker LbL blends are still higher than that of the BHJ devices with similar blend thicknesses.

2.4.2. Simulated photoabsorption rate in devices. To visualize the modulation of the electric field inside the BHJ and LbL layers, we depicted the field distribution for the wavelength range of 350–900 nm. The results for the BHJ and LbL devices with an active layer thickness of 125 nm are depicted in Fig. 4d and e, respectively. The analysis of the photon absorption rate profile within the different BHJ and LbL layers was performed using the optical transfer model. Note that this model is an invaluable tool in understanding where to assess the likely optical impacts of changing the blend ratios and morphologies.[50,52] As shown, the photon absorption profiles are relatively uniform over the active layer region in the BHJ and LbL devices. In general, Fig. 4d and e can be viewed as the charge generation profile within the BHJ and LbL devices if most of the photons absorbed in the films can be effectively separated into free charges, respectively. The generation of free charges is mainly concentrated near the anode side in both devices. More importantly, the photon absorption rate profile of the LbL layer is slightly stronger than that of the BHJ layer, which is consistent with the enhancement results shown in Fig. S1 and S6 (ESI†).

As a result, the improved J_{sc} originated from the optimized vertical stratification of the active layers depicted in Fig. 3g, which play a crucial role in the optical distribution. Besides the optical simulations of the BHJ and LbL blends, to discern the influence of two different morphologies on the charge generation and extraction dynamics, transient dynamics studies over the femtosecond to microsecond time scales were explored in the following section.

2.5. Physical dynamics

The photovoltaic parameters (Table S1, ESI†) of the BHJ and LbL blends are affected by several fundamental processes associated with the conversion of light (photons) into current (extracted charges at the electrodes). Moreover, the variation in the BHJ and LbL blend morphologies as mentioned above is particularly significant since it changes the interfacial area between the D and A materials, and vertical phase separation and traps or defect densities. Consequently, it can cause changes in the exciton dissociation and carrier dynamics, and therefore provide more insight into the reasons for the observed performance trends. Thus, we performed a stepwise characterization of the exciton dynamics, charge generation, transport, and collection processes in the BHJ and LbL blends by employing steady-state and transient spectroscopic techniques.

2.5.1. Exciton dynamics. Photoluminescence (PL) quenching provides direct evidence for exciton dissociation, and the degree of PL quenching reflects the efficiency of the exciton dissociation, which is an effective measure of the efficiency of converting excitons into charge carriers.[53] To understand the limitations of the BHJ and LbL blends, we firstly measured the steady-state PL spectra of the neat films of J71 and ITC6-IC as well as their blended BHJ and LbL films upon excitation at 400 nm. Notably, the PL intensity of J71 decreased significantly when ITC6-IC was added, as seen in Fig. S8a (ESI†). The relevant quenching efficiencies are summarized in Table S1 (ESI†). The PL quenching was approximately 90% for the BHJ blend and 93% for the LbL blend, indicating that most of the generated excitons (photons absorbed) are available for charge generation.

To gain further insight into the exciton diffusion, we monitored their dynamics *via* time-resolved PL (TRPL) spectroscopy. These measurements were carried out by exciting the ground state absorption of the J71 donor (Fig. S1, ESI†) and probing the decay of the J71 PL using a streak camera system. Fig. S8b (ESI†) shows the PL intensity decay of the neat J71 and ITC6-IC films in comparison to their BHJ and LbL thin films. The data indicates a very efficient reduction of the PL in both architectures. As indicated by the steady state spectra, the emission from the J71 donor was almost completely quenched, whereas a much reduced, but finite emission from the donor remained visible in both the BHJ and the LbL films. The extracted lifetimes of the PL decay at a maximum emission showed a drastic reduction for the blends (16–18 ps), which indicates that the excitons dissociate quickly after their generation and none of the systems are diffusion limited. Furthermore, it was noted that the more efficient quenching of the J71 PL may be aided by an additional Förster-type transfer process.[54] Thus, the energy transfer in the J71:ITC6-IC system may further explain the differences observed in the EQE spectra.

2.5.2. Charge generation. As shown in recent studies,[47–51] the ability of charges to rapidly move away from the donor–acceptor interface plays a major role in efficient charge generation. Thus, we further investigated the exciton relaxation dynamics of the BHJ and LbL blends using femtosecond transient absorption spectroscopy (TAS). Fig. 5a–d show the spectro-temporal TA maps of the pristine J71 film, ITC6-IC film, BHJ, and LbL blends, respectively. To observe the hole injection dynamics from ITC6-IC to J71 in the blends, the TA spectra were measured under a low excitation fluence (45 μJ cm^{-2}), and all the samples were pumped by 640 nm (1.95 eV) laser pulses. Note that the photoinduced transmission changes, $\Delta T/T$, of all the samples are positive, representing the bleach of the lowest exciton state. As shown in Fig. 5a, no decay of the TA signal intensities for the J71 film was observed in the timescale up to 100 ps. In contrast, a significant decay in the TA single intensities was found in the pristine ITC6-IC film (Fig. 5b). In the same intensity scale, we further found that the TA signal intensity decay for the LbL bend (Fig. 5d) was faster than that of the BHJ blend (Fig. 5c) under the same excitation fluence. This result indicates that a more efficient hole transfer channel existed in the LbL blend compared to its BHJ counterpart. Furthermore, we monitored the charge separated polaron dynamics (592 nm) of both blended films (Fig. 5e), which indicated the more effective transport of holes in the LbL blend. We also calculated the hole injection rate constant (k_{inj}), *i.e.*, hole injection time, by fitting the TA decay curves with a single exponential function. Notably, the fitting results reproduced the experimental results well (Fig. 5e).

The hoe injection efficiencies in both the BHJ and LbL morphologies can be calculated according to the equation $\eta_{inj} = k_{inj}/(k_{inj} + k_{rec})$,[55,56] where, η_{inj} is the hole injection

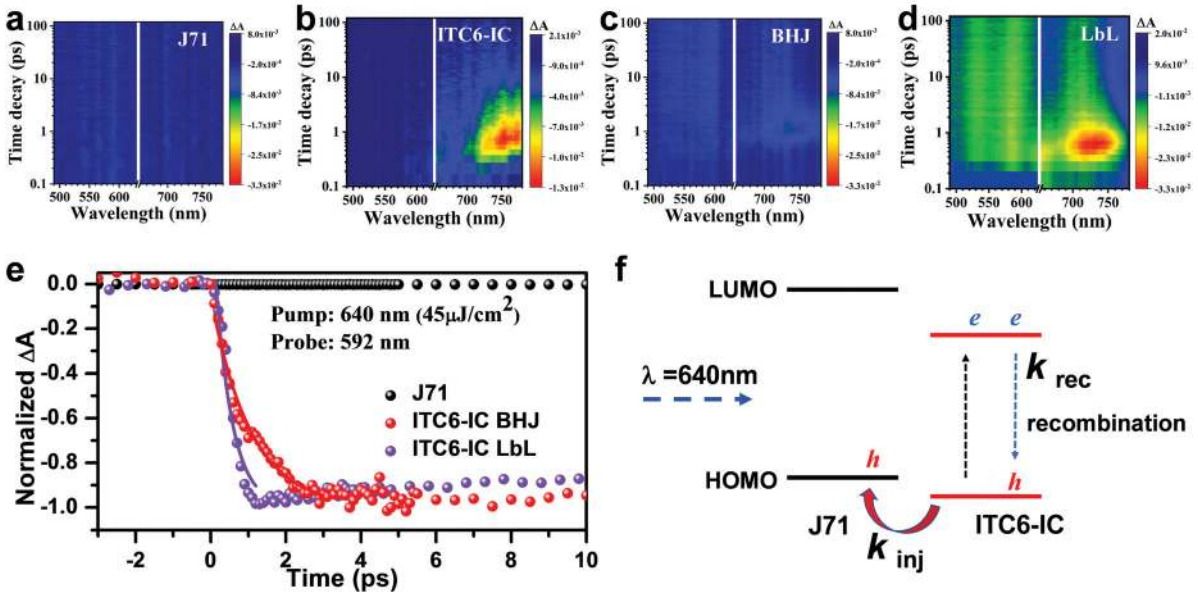

Fig. 5 fs–ns transient dynamics for the pristine (a) J71 and (b) ITC6-IC films and their (c) BHJ and (d) LbL blends pumped at 640 nm and monitored at the same intensity scale of time decay. (e) fs–ns transient dynamics for the BHJ and LbL blends pumped at 640 nm and monitored at 592 nm. The solid lines represent the multiexponential fitting of these dynamics. (f) Schematic illumination of the hole injection dynamics from ITC6-IC to J71 for the BHJ and LbL blends.

efficiency in the blend film and k_{rec} is the charge recombination rate. In the BHJ blend, η_{inj} was estimated to be as high as 89.7%. The higher phase separation is probably the reason for the efficient "hole injection efficiency" in the BHJ blend. Interestingly, the η_{inj} of the LbL blend was 95.3%, which is higher than that of the BHJ blend. This indicates the more efficient exciton diffusion and charge generation in the LbL morphology with a p–i–n like structure, as depicted in Fig. 3g.

Both the BHJ and LbL blends were also pumped by 470 nm (2.64 eV) laser pulses to investigate the photoinduced electron transfer from the donor to acceptor (Fig. S9, ESI†). As shown in Fig. S9d (ESI†), no bleach was found in the region of 500–600 nm in the LbL blend, indicating that the photoexcited electrons in J71 were injected into ITC6-IC very fast at less than 1 ps. In contrast, as provided in Fig. S9c (ESI†), there was a small bleach signal, which suggests the injection of photo-excited electrons from J71 to ITC6-IC in the case of BHJ is a little slower compared to that of the LbL blend. In addition, as shown in Fig. S9f and g (ESI†), it was also found the bleach signals of the LbL blend at 730 nm were stronger than that of the BHJ blend, indicating that more photoexcited electrons from J71 to ITC6-IC were injected in the LbL blend. These results are consistent with the PL quenching efficiencies of both blends, which also indicate reasonably efficient exciton dissociation in the LbL blend.

We also studied the charge photo-generation of the relevant devices by examining the photocurrent at the saturation point where the internal field is large enough to sweep all the carriers to the electrodes prior to recombination. Fig. S10 (ESI†) shows the photocurrent density (J_{ph}) *versus* the internal voltage (V_{in}) of the devices for the BHJ and LbL systems under illumination at 100 mW cm^{-2}. Here, we expect that almost all of the photo-generated free charges within both systems are collected at higher V_{in} (>3 V). Moreover, we found that the J_{ph} at V_{in} = 4 V is about 18.49 mA cm^{-2} for the LbL device. However, the J_{ph} at the same V_{in} is only 17.28 mA cm^{-2} for the BHJ device. On one hand, just a small portion of the large J_{sc} losses of the BHJ device compared to the LbL device can be explained by the poor optical properties of the optimal BHJ blend, as discussed in Fig. 4. On the other hand, the loss in J_{sc} in the BHJ device may be partially attributed to its unbalanced and poor charge carrier transport and increased non-geminate recombination. These assumptions will be experimentally verified in the next section.

2.5.3. Charge transport properties. To investigate the effects of the BHJ and LbL morphologies on the charge transport properties, we firstly performed space charge limited current (SCLC) measurements on representative BHJ and LbL hole-only devices, as presented in Fig. S11 (ESI†). The hole mobilities were 4.66 $\times$ 10^{-4} cm^2 V^{-1} s^{-1} for the BHJ blend and 3.75 $\times$ 10^{-4} cm^2 V^{-1} s^{-1} for the LbL blend. The hole mobility values of the LbL hole-only diodes were slightly lower than that of the BHJ system, which is probably due to their different vertical phase separation. More acceptor materials were enriched on the top of the LbL blend, as depicted in Fig. 3g, which can inevitably suppress the delivery of holes.[36] In addition, we also employed photo-induced charge carrier extraction by linearly increasing the voltage (photo-CELIV) over the nanosecond–microsecond (ns–μs) time regime to determine the ambipolar charge extraction from an actual photovoltaic device. Fig. 6a shows the photocurrent transients recorded by applying a 2 V/40 μs linearly increasing reverse bias pulse to the BHJ and LbL solar cells after a 1 μs delay time. To determine the mobility,

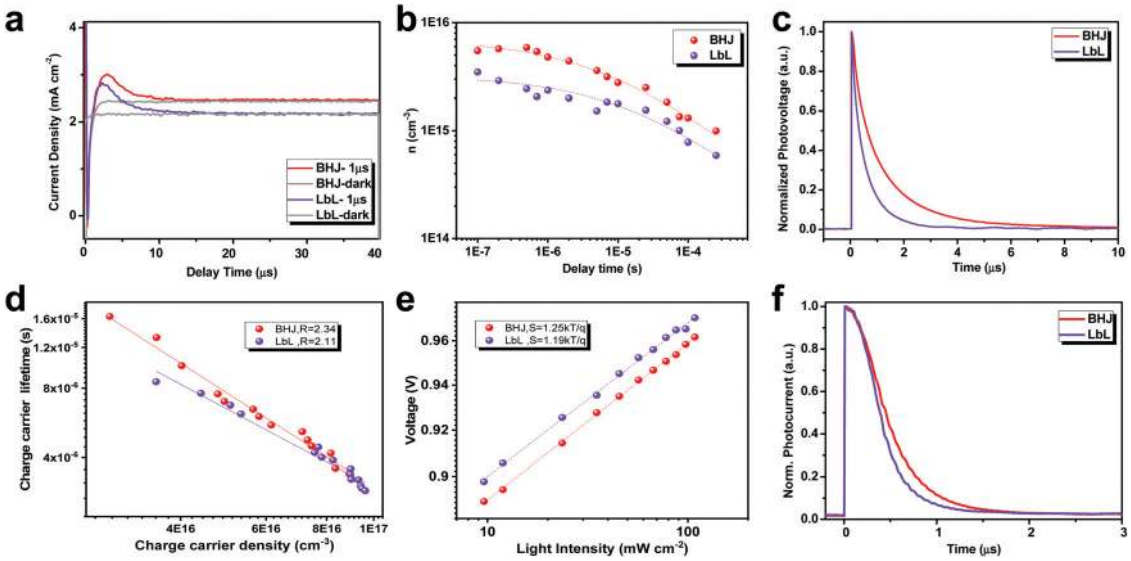

Fig. 6 (a) Photo-CELIV traces for the BHJ and LbL devices after a delay time of 1 μs. The dark CELIV traces are also shown. (b) Number of extracted carriers as a function of delay time and the fit. (c) Transient photo-voltage measurements of the BHJ and LbL devices. (d) Charge carrier lifetime obtained from TPV as a function of charge carrier density (n), calculated from CE measurements under V_{oc} conditions. The solid lines represent linear fits of the data. (e) Voltage *vs.* light intensity of the relevant devices. Intensities were corrected for AM1.5G spectral mismatch. (f) Normalized TPC data for the BHJ and LbL solar cells. The illumination pulse intensity was 150 mW cm^{-2} (light pulse of 50 μs).

fourteen photo-CELIV curves were recorded using different experimental conditions for each sample, differing in delay time and applied voltage (Fig. S12, ESI†). The average mobilities in the devices are provided in Table S5 (ESI†). The average mobility of the LbL device (1.62×10^{-4} cm^2 V^{-1} s^{-1}) was higher than that of the BHJ device (8.41×10^{-5} cm^2 V^{-1} s^{-1}). Thus, it can be concluded that charge carriers can be transmitted more efficiently in a real LbL device.

2.5.4. Charge carrier recombination and extraction. The time-dependence of the charge carrier density was also studied to investigate the recombination mechanisms of the charge carriers in the BHJ and LbL blends. As shown in Fig. 6b, the number of extracted carriers was reduced with an increase in delay time between photogeneration and extraction due to the various recombination processes in the devices. Furthermore, using the following equation: $(n(t) = n(0) \Big/ \left(1 + \left(\frac{t}{\tau_B}\right)^{\gamma}\right)$, where, $n(0)$ is the initial density of photogenerated carriers at $t = 0$ and γ is the time-independent parameter), the effective 2nd order recombination coefficient (τ_B, known as bimolecular recombination coefficient) was calculated.[49] The relevant parameters fitted and calculated by the abovementioned equation are summarized in Table S5 (ESI†). It is strange that the initial density of the photogenerated carriers in the BHJ blend is higher than that of the LbL blend, which is probably due to their different vertical phase separation. The laser shone directly into the anode electrode (ITO (indium tin oxide)/PEDOT:PSS (poly(3,4-ethylenedioxythiophene)polystyrene sulfonate)) and passed through the active layer. Consequently, more photogenerated carriers were generated in the BHJ blend, which also explains its shorter bimolecular recombination coefficient (5.59×10^{-5} s for the BHJ blend and 1.31×10^{-4} s for the LbL blend). We further calculated the transient time t_{tr} ($t_{tr} = d^2/\mu V$, where, d is the film thickness).[36] The t_{tr} values are 2.38×10^{-7} s for the BHJ device and 1.23×10^{-7} s for the LbL device. This result is also identical to the transient photovoltage (TPV) measurements, as presented in Fig. 6c. The BHJ device showed a carrier lifetime of 3.4 μs when the light intensity was around 2.5 suns, whereas the lifetime of the J71/ITC6-IC system using the LbL structure decreased to 2.8 μs at the same intensity. This may be ascribed to less charge recombination and fewer traps within the LbL blend supported by the above-discussed morphology characterizations and the light intensity dependence of the open-circuit voltage (V_{oc}) and J_{sc} data discussed next. Additionally, as shown in Table S5 (ESI†), the longer drift length of the charge carriers (l_d = 466 nm, l_d is the mean distance over which the charges can move before significant recombination occurs) indicates that carriers are able to travel significantly longer distances in the LbL blend without considerable recombination compared to in the BHJ blend (l_d = 379 nm).

To directly determine the carrier recombination in these two blends, we combined the TPV and CE techniques to yield the charge carrier lifetime, τ, as a function of charge carrier density under open circuit conditions, $\tau(n)$ (Fig. 6d).[36] Note that the τ and n values in the BHJ- and LbL-treated devices are comparable. Here, a non-geminate recombination order R ($R = \lambda + 1$) was calculated *via* the equation $\tau = \tau_0(n_0/n)^{\lambda}$, where, τ_0 and n_0 are constants and λ is the so-called recombination exponent.[5,57] Generally, a recombination order higher than two is attributed to the effect of trapping and release in energetic traps, as well as morphological traps.[10,44,46] As shown in Fig. 6d, a slightly higher recombination order value (R = 2.34) for the BHJ device compared to the LbL device (R = 2.11) was observed. In addition, multiple studies have demonstrated that the light

intensity dependence of the V_{oc} can directly provide insight into the role of trap-assisted recombination *versus* 2nd order recombination at the open circuit condition. The V_{oc} and light intensity (I) can be correlated by the expression[46] $V_{oc} = \frac{E_{gap}}{q} - \frac{kT}{q}\ln\left[\frac{(1-P)\gamma N_c^2}{PG}\right]$, where, E_{gap} is the energy difference between the highest occupied molecular orbital (HOMO) of the electron donor and the lowest unoccupied molecular orbital (LUMO) of the electron acceptor, q is the elementary charge, k is the Boltzmann constant, T is the temperature in Kelvin, P is the dissociation probability of the electron–hole pairs into free carriers, γ is the recombination constant, N_c is the density of states in the conduction band, and G is the generation rate of electron–hole pairs. Following the rules, this formula predicts a slope $S = (kT/q)$ for V_{oc} *versus* the natural logarithm of the incident light intensity. This implies that the slope of V_{oc} *versus* $\ln(I)$ is equal to kT/q for 2nd order recombination. When trap-assisted recombination is involved, a stronger dependency of V_{oc} on the light intensity is observed. As shown in Fig. 6e, the LbL device exhibited a logarithmic dependence on light intensity with a slope of 1.19 kT/q, which is close to kT/q for a 2nd order recombination process. Moreover, the slope yields 1.25 kT/q for the BHJ device, implying that the poor BHJ blend may cause a number of trapping defects, which likely contribute to the trap-assisted recombination in this blend.

Now, the remaining question is to evaluate the influence of the two different morphologies on the charge collection efficiency and the dwell time of charges in the active layer prior to charge extraction at the electrodes. Here, we conducted transient photocurrent (TPC) measurements on the devices under the short circuit condition. Fig. 6f exhibits the charge extraction of the BHJ and LbL devices at J_{sc} condition, where the internal field equals the V_{bi}. The extraction time of the BHJ device was extracted to be τ = 0.41 μs. In the case of the LbL device, it showed a very short lifetime of around 0.30 μs. The shorter extraction lifetime suggests that photo-generated carriers are extracted more efficiently in the LbL devices than the BHJ devices. These results also imply that the difference in FF observed in the BHJ and LbL blends (Fig. S15, ESI†) is not only a consequence of different non-geminate recombination rates, but also the rate of charge extraction. Briefly, the results of the carrier recombination dynamic analysis coupled with the voltage dependence of the non-geminate recombination and charge carrier mobilities finally underpin the complex morphology outlined above and give detailed insight into the subtle mechanisms responsible for the device parameters.

3. Discussion

The choice of processing conditions based on the BHJ and LbL approaches enables the D/A interfacial area to be changed, fine-tuning the molecular ordering and vertical phase separation. Consequently, it is likely to cause changes in the fundamental photo-physical processes, as depicted in Fig. 4–6. We suggest that the LbL approach can effectively suppress the bulk recombination and reduce the number of traps or defects. In this section, we further evaluate the BHJ and LbL technologies, discuss the relationships between blend morphology, physical dynamics, photovoltaic parameters, and device stability, and give real insight into which approach is more suitable for the large-area fabrication of OSCs in commercial applications.

3.1. Nanoscale morphology and its origin

Fig. 3g schematically shows the nanoscale morphology of the two blends, with the main difference being the composition of the vertical phase. In general, vertical stratification of electron donors and acceptors during their thin-film-formation process is a complex process resulting from the synergistic effects of thermodynamics, kinetics, free-surface or interfacial surface energy, interface effects, centripetal forces, chemical reaction between the active layer and substrate, *etc.* The processing conditions,[58–63] such as the solubility of the D and A materials, solvent evaporation rate, interaction between components, liquid and solid additives, post-treatments, free energies of the components, surface of the substrates and device architecture, can all be effective in tuning the final film morphology. In the film formation of the BHJ blend, phase separation will occur due to the reduced solubility of D and A, and the interactions between the D materials, A materials, and solvent. Changes in the film drying time (or rate of solvent evaporation) should have an impact on the vertical stratification in photovoltaic blends.[64] The failure of quick diffusion of solvent molecules from the bottom to the top to supplement the concentration will lead to the formation of a "skin" in the partly wet film, and substantially postpone the rest of the drying process. This indicates that any lateral or vertical morphology that is formed during the film-formation process of the BHJ blend may be a kinetics-limited state, which can be controlled by the selective dissolubility and free energies of the donors, acceptors, and substrate surface. Thus, it is very difficult to obtain ideal vertical profiles using the BHJ method.

In contrast to the BHJ blend (Fig. 3g), the donor material is enriched in the bottom of the LbL blend, and the acceptor material is enriched in the upper layer. From this analysis, we further conclude that the LbL processing approach primarily acts as a plasticizer to enable ripening of the domains, aggregation of the molecules, and eventually vertical phase separation. The LbL layer is formed by doctor-blading a solution of acceptor materials on the corresponding dry film only containing the donor materials. Consequently, deposition onto the pristine donor films held at different temperatures enables different film drying times, and therefore kinetically allows different times for component diffusion and stratification. Furthermore, a high-quality LbL morphology with a p–i–n like vertical structure can be achieved by adjusting the blade speed and substrate temperature, resulting in superior PCEs in LbL devices compared to that of BHJ devices. Although the abovementioned factors including thermodynamics, kinetics, surface free energy and selective dissolubility still possibly influence the vertical phase components, the LbL approach itself is the main origin of the vertical stratification. Thus, unlike the BHJ method, in which the optimization of the active layer is mainly implemented through trial-and-error experimental routines,

LbL technology is a more rational controlled approach for vertical stratification to obtain high-performance OSCs.

3.2. Structure governing device dynamics and efficiencies

It is well accepted in the OSC community that film microstructures and aggregation at molecular length-scales as well as vertical phase separation play critical roles in controlling the optoelectronic properties *via* their effects on light absorption, exciton dissociation, charge generation, carrier transport, and recombination. Thus, the growing understanding of the use of processes to control morphology and tune physical dynamics through BHJ and LbL processing methods should be highlighted. This will allow rapid progress to be made in the development of highly efficient OSCs.

Based on the morphology analysis from GIWAXS and TOF-SIMS measurements, it is convincing that the increase in D/A aggregations in the LbL blend is directly reflected in the diffraction data. The impact of morphology on the device performance, especially on J_{sc}, partially depends on the absorption coefficient of the active layers and the photoabsorption rate of the devices. Importantly, both the BHJ and LbL blends show suitable miscibility of the donor and acceptor materials, as demonstrated by the above-mentioned PL and TRPL as well as the saturated photocurrent density measurements. Thus, there is no common morphological limitation that impacts exciton dissociation and charge generation, which was demonstrated by the similar saturated photocurrent densities in the BHJ and LbL devices (Fig. S10, ESI†). In the BHJ devices, charge trapping in pure domains is not an issue because the J71 polymer entanglements enable connectivity for charges throughout the BHJ blend even down to J71 compositions of a few volume percent. However, the BHJ blend with small, mixed domains shows higher D : A miscibility compared to the LbL blend, which increases the probability of charge trapping and carrier recombination.

Interestingly, the LbL active layer with suitable vertical phase separation and highly crystalline domains preserved the interfacial exciton harvesting and even showed a higher hole injection efficiency and ultrafast charge generation, which were supported by the TA measurements. On one hand, we propose that in the LbL blends, a possible target goal will be high miscibility to ensure mixed phases that promote charge percolation through the minority component, but maintain the ability of the majority component to aggregate (Fig. 3g). On the other hand, due to the uniqueness of non-fullerene materials,[65] the further enhancements to their diffusion lengths may even obviate the need for the bulk heterojunction morphology. Thus, our results provide impetus for further measurements on other BHJ and LbL blends to probe the generality of these morphology guidelines to maximize their performance.

Besides the requirements of small, highly ordered crystallites or aggregated domains in an ideal active layer, suitable vertical phase separation is also essential, which significantly affects all stages of charge generation, especially charge transport and extraction. An unsuitable vertical phase with a small-scale BHJ blend limits p-type and n-type domain connectivity for charge transport in devices, even though it shows a slightly high hole-only mobility. Indeed, the space-charge build-up measured *via* TPC for the BHJ devices goes hand-in-hand with the pure disconnected BHJ domain, resulting in large populations of bound geminate pairs and charges trapped in domain islands. Moreover, even when the BHJ blend is optimized, non-geminate recombination losses from trapping continue to play a significant role in the BHJ systems, as discussed above. Consequently, TPC charge extraction remains low in the optimized BHJ device, consistent with charges being spatially trapped in unsuitable vertical phase separation. In contrast, with an improvement in vertical phase separation *via* the introduction of the LbL approach during film formation, improved charge transport and extraction prevail over the extra carrier losses in devices. This explains the concurrent increase in J_{sc} and FF values compared with the BHJ system, despite the LbL blend having good mixing propensity and high PL quenching efficiency. As depicted in Fig. 3g, D/A mixing in the intermediate domain while retaining slightly larger pure domains at the top and bottom sides is not only beneficial for exciton diffusion and dissociation, but also can be linked to reduced charge recombination. The total carrier recombination losses in OSCs is determined by the competition between recombination and extraction. Several studies have demonstrated that identifying high domain purity is important to maintain low recombination rates by separating charges into spatially segregated domains.[4,49,66] Thus, direct, trap-free charge percolation routes through mixed phases and efficient π–π stacking close to opposite ends are the likely reasons for the low non-geminate recombination losses observed in the LbL blends.

Overall, we showed that the BHJ devices exhibit slower charge generation, more carrier trapping, and poorer extraction compared to the LbL solar cells. A suitable vertical phase separation will likely translate into a decrease in recombination losses and an increase in charge mobility across the active layer, leading to slightly higher J_{sc} and FF values in the LbL devices. Consequently, the PCEs of the J71:ITC6-IC system can increase from 10.41% for the BHJ-bladed blend to 11.47% for the LbL-bladed blend, which are also similar with that reported for a spin-coated BHJ blend.[47] Two points should be highlighted here for the comparison of the coating approaches. On one hand, engineering the local molecular orientation and crystallinity at the interfaces between the active layer and electrodes is a likely pathway to an efficiency improvement in BHJ devices.[67] On the other hand, although suitable vertical phase separation can be easily achieved *via* the LbL approach, the lack of control over crystal size during solution processing remains a key limitation.

3.3. Structure deciding energy loss of blend

Besides the J_{sc} and FF values, we also found that the LbL approach could efficiently reduce the energy loss of the J71:ITC6-IC system. As shown in Table S1 (ESI†), the BHJ device with a V_{oc} of 950 mV showed an energy loss of 0.72 eV, while the LbL blend with a V_{oc} of 968 mV provided a smaller energy loss of 0.702 eV. The better vertical phase-separated morphology of the LbL blend can effectively narrow the shape of the density of state (DOS).[68] Thus, the corresponding electron quasi-Fermi level (E_{Fn}) of the acceptor can be up-shifted, meanwhile the hole quasi-Fermi level (E_{Fp}) will be down-shifted,[69] as depicted in Fig. S16 (ESI†).

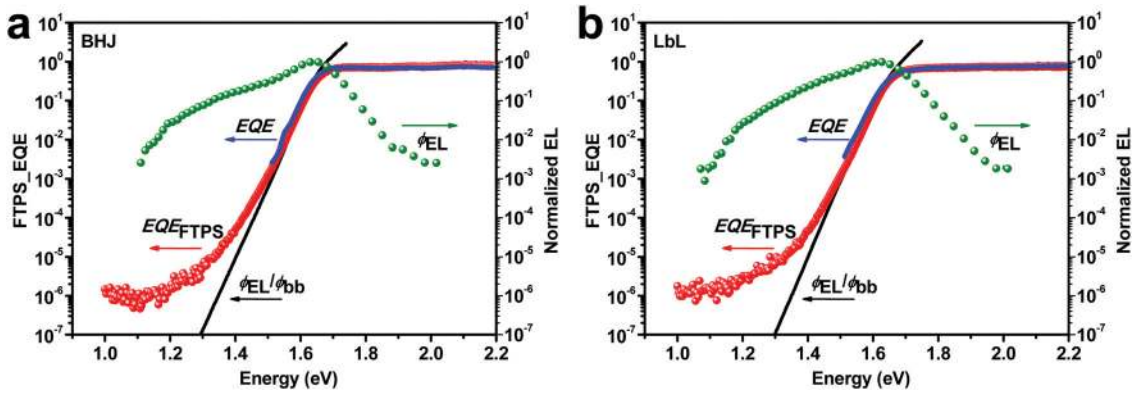

Fig. 7 FTPS-EQE (red lines) and EL (green lines) spectra of the (a) BHJ and (b) LbL blade-coated OSCs.

Table 1 Summary of the parameters measured and calculated from FTPS-EQE and EL

Blends	E_{gap} [a] (eV)	V_{oc} [b] (V)	E_{loss} [c] (eV)	V_{oc}^{SQ} [d] (V)	V_{oc}^{rad} [e] (V)	$q\Delta V_{oc}^{rad}$ [f] (eV)	$q\Delta V_{oc}^{non\text{-}rad}$ [g] (eV)
BHJ	1.67	0.955	0.715	1.38	1.326	0.054	0.371
LbL	1.67	0.971	0.699	1.38	1.326	0.054	0.355

[a] E_{gap}: the band gap (1.67) of ITC6-IC was determined from the crossing point between its emission and absorption spectra, as presented in Fig. S17 (ESI). [b] Voltage values calculated for J71:ITC6-IC devices based on the BHJ and LbL blends. [c] V_{oc} loss is equal to the difference in E_{gap} and V_{oc}. [d] V_{oc}^{SQ}: Schokley–Queisser limit to V_{oc}. [e] V_{oc}^{rad}: radiative limit to V_{oc}, measured using EQE–EL. [f] ΔV_{oc}^{rad}: voltage losses due to non-ideal absorption (calculated from EL and FTPS measurements). [g] $\Delta V_{oc}^{non\text{-}rad}$: voltage losses due to non-radiative recombination only.

In addition, the preferable way of quantifying the energy and voltage losses in OSCs is to use the detailed balance theory, as described in the ref. 70 and 71. Following the Shockley–Queisser (SQ) limit, the voltage losses ($q\Delta V_{oc}$) can be categorized into three different terms ($q\Delta V_{oc} = (E_{gap} - qV_{oc}^{SQ}) + (q\Delta V_{oc}^{rad}) + (q\Delta V_{oc}^{non\text{-}rad})$).[71] We quantified the energy and voltage losses by characterizing the Fourier-transform photocurrent spectroscopy external quantum efficiency (FTPS-EQE) and electroluminescence (EL) spectra for the investigated solar cells, as presented in Fig. 7. The calculation results are summarized in Table 1. Both the BHJ and LbL devices showed the same $\Delta E_1 = E_{gap} - qV_{oc}^{SQ}$ with a value of 0.29 eV and $\Delta E_2 = q\Delta V_{oc}^{rad}$ with a value of 0.054 eV. The third loss $\Delta E_3 = q\Delta V_{oc}^{non\text{-}rad}$ is the difference between qV_{oc}^{rad} and the measured qV_{oc} under AM1.5G simulated solar spectrum. The LbL solar cells gave an extremely smaller $q\Delta V_{oc}^{non\text{-}rad}$ of 0.355 V compared to that of the BHJ devices (0.371 V). The smaller $q\Delta V_{oc}^{non\text{-}rad}$ value in the LbL solar cell indicates that the LbL approach has a great role in reducing non-radiative recombination, which was demonstrated by the above-mentioned physical measurements. Overall, replacing BHJ with the LbL process for the film formation of the active layer can further modify the DOS, while inducing better Fermi level alignment with the electrodes, reducing non-radiative recombination, and thus increasing the V_{oc} of the relevant devices to a significant extent.

3.4. Structure-influencing stability issues

Our results are very interesting since the device performance only improved slightly for the LbL blend when the LbL blend showed a dramatically different vertical phase separation compared with the BHJ blend. This drove us to further explore the stability issues of OSCs, which generally are controlled by the blend microstructure.[4] In the following section, we systematically investigated the stability issues of the BHJ and LbL blends, including photo-stability, thermal stability, and mechanical stability.

3.4.1. Photo-stability of BHJ and LbL blends. Many studies have shown that enhanced donor crystallinity and suitable phase separation can improve the device photo-stability. However, few reports have depicted the correlation between the vertical phase separation and device stability. Based on this, we explored the long-time light-induced stability of the BHJ and LbL devices tested in a nitrogen glovebox at room temperature. Fig. 8a shows the relative change in the recorded PCEs of the BHJ and LbL devices. The BHJ device showed a PCE degradation down to 68% within 500 h, while the LbL device showed the lowest PCE loss down to *ca.* 85% during the same period. Furthermore, the BHJ blend showed poorer stability with a light-induced PCE degradation of around 32% after 500 h, mainly resulting from J_{sc} and FF losses (Fig. S18, ESI†). The LbL system was more stable under illumination within 500 h compared to the BHJ system. Here, we correlate the higher light stability with the suitable vertical phase separation with enhanced donor and acceptor aggregations.[72] Notably, the degradation behavior depends strongly on the approach used for film formation while all other factors are the same. Further GIWAXS measurements (Fig. S19 and S20, ESI†) demonstrated that the D and A materials were separated in the BHJ blend, and thus formed large domains, which resulted in the obvious burn-in loss.

3.4.2. Thermal stability of BHJ and LbL blends. Besides light, accumulated heat from illumination is unavoidable, which can severely change the optimized blend morphology in a short time and further significantly lead to PCE losses.[72,73] This is why an optimal morphology generally is a metastable state, and further moves toward to a thermodynamic equilibrium

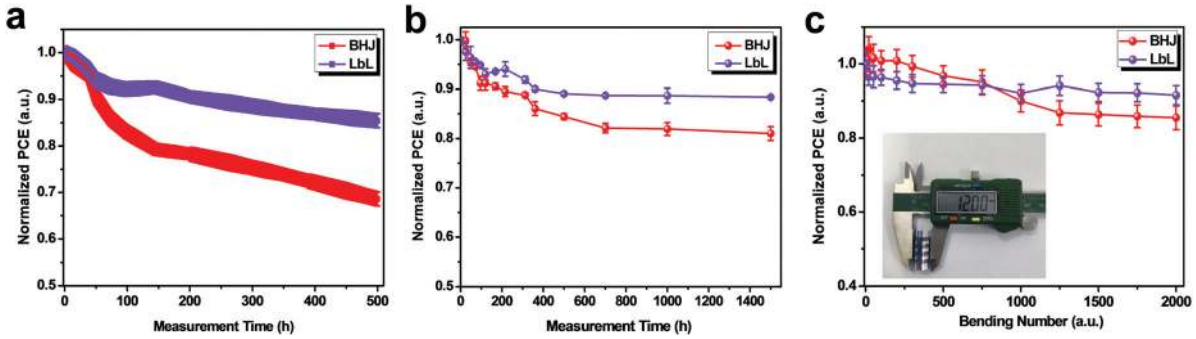

Fig. 8 (a) Variation in the normalized average PCE losses over illumination time over 500 h for the BHJ and LbL devices based on ITO/PEDOT:PSS/BHJ or LbL/PDINO/Ag measured in a dry nitrogen atmosphere. (b) Variation of normalized PCE of the BHJ and LbL devices annealed at 120 °C over 1500 h. (c) Bending test of the flexible BHJ- and LbL-based OSCs. The inset shows a photo of the bending instrument with a radius of 6 mm.

state to form large phase separations, mainly accelerated by the accumulated heat. Thus, this prompted us to investigate the thermal stability of the BHJ and LbL blends to check which processing method is more suitable to meet the requirements of thermal stability in OSCs. Here, better thermal stability was also found for the LbL blend compared to the BHJ blend. As shown in Fig. 8b, the BHJ device exhibited a rapidly decreasing device performance upon continuous annealing and maintained 81% of its initial PCEs after baking at 120 °C under an inert atmosphere for 1500 h. It should be noted that the thermally induced degradation of the BHJ blend was mainly due to the degradation of J_{sc}, probably resulting from the huge changes in the blend morphology, as demonstrated by the GIWAXS measurements (Fig. S19, ESI†). In contrast, the device performance of the LbL devices maintained 88% of its initial performance, probably due to the very stable blend morphology (Fig. S20, ESI†). Compared to the BHJ blend, the LbL morphology barely changed after baking at 120 °C for 1500 h.

3.4.3. Bending stability of BHJ and LbL blends. As expected, the LbL processing technology also affords a new opportunity in flexible OSCs. The BHJ and LbL blends showed different vertical phase separation, which probably also influenced the mechanical stability of the relevant active layers. Thus, we also measured the bending stability of the BHJ and LbL blends, as shown in Fig. 8c, which exhibits the normalized PCEs of the BHJ and LbL devices as a function of bending cycles with a radius of 6 mm. The BHJ-coated flexible device based on the configuration of polyethylene terephthalate (PET)/ITO-metal-ITO (IMI)/PEDOT:PSS/active layer/PDINO/Al retained approximately 85% of its initial PCE after 2000 bending cycles, while the LbL-bladed device showed 92% of its initial PCE under the same conditions. Thus, the more stable blend morphology for the application of rigid and flexible OSCs and solar modules was achieved *via* the LbL processing approach, which can effectively reduce the efficiency-stability gap.

4. Conclusion

In summary, we first conducted an in-depth study on the film formation, optimization, and degradation processes of J71:ITC6-IC doctor-bladed blends fabricated *via* two different processing technologies, BHJ and LbL. Furthermore, we correlated the different 3D morphological characteristics to the photocurrent generation and extraction processes of the BHJ and LbL blends as well as their stability issues in devices. After this comprehensive study, it was found that the LbL blade-coating process exhibits many advantages over the widely used BHJ method.

The details are as follows: firstly, compared to the BHJ blade-coating technology, the LbL blading approach not only facilitates ITC6-IC acceptor molecules to mix with the J71 donor for achieving a thermodynamically more favorable nanomorphology with suitable D/A interface area, but also improves the formation of larger, separated D/A domains, and the segregation of acceptors towards the top of the active layer. This desired hierarchical morphology can be easily obtained by independently controlling and optimizing the D and A deposition, indicating that the LbL solution processing technique is a promising and cost-effective strategy. Secondly, the 3D geometry of the LbL blend compared to that of the BHJ blend allows for achieving a higher light absorption coefficient, and thus improved charge generation in the active layer. Thirdly, the suitable morphologies and interfaces between donors and acceptors can effectively provide a strong charge transfer driving force and small energy loss of charge transfer simultaneously. Meanwhile, the p–i–n like structure is also beneficial for charge transport and collection at the appropriate electrodes, and thus non-geminate recombination can be further reduced. Thus, the films fabricated with the J71:ITC6-IC system yielded a 10% increment in PCE with the LbL doctor-bladed approach. Finally, the LbL blend with a suitable vertical phase separation exhibited a more stable morphology than that of the BHJ blend. As expected, the relevant LbL bladed systems can meet the requirements of long-term irradiation and thermal stability as well as compatible mechanical stability in flexible devices.

Overall, our work demonstrates that the LbL blade-coating approach is a promising strategy and even a superior alternative to the BHJ method for controlling the blend morphology, and presents good generality, high efficiency, and good stability. We also hope researchers will focus more on this coating technology.

Conflicts of interest

There are no conflicts to declare.

Acknowledgements

This work was financially supported by the National Natural Science Foundation of China (Grant No. 21702154 and 51773157). We also thank the support of the opening project of Key Laboratory of Materials Processing and Mold. L. Y. and H. A. were support by the US Office of Naval Research (ONR, Grant No. N000141712204). TOF-SIMS was performed at the Analytical Instrumentation Facility (AIF) at NCSU, which was supported in part by the State of North Carolina and the National Science Foundation (Award No. ECCS-1542015). S. K. acknowledges the Deutsche Forschungsgemeinschaft for the award of a personal fellowship (408012143).

References

1 K. Zhou, J. Xin and W. Ma, *ACS Energy Lett.*, 2019, **4**, 447–455.
2 F. Zhao, C. Wang and X. Zhan, *Adv. Energy Mater.*, 2018, **8**, 1703147.
3 L. Ye, H. Hu, M. Ghasemi, T. Wang, B. A. Collins, J. H. Kim, K. Jiang, J. H. Carpenter, H. Li, Z. Li, T. McAfee, J. Zhao, X. Chen, J. L. Y. Lai, T. Ma, J. L. Bredas, H. Yan and H. Ade, *Nat. Mater.*, 2018, **17**, 253–260.
4 J. Min, X. Jiao, V. Sgobba, B. Kan, T. Heumüller, S. Rechberger, E. Spiecker, D. M. Guldi, X. Wan, Y. Chen, H. Ade and C. J. Brabec, *Nano Energy*, 2016, **28**, 241–249.
5 J. Min, N. S. Güldal, J. Guo, C. Fang, X. Jiao, H. Hu, T. Heumüller, H. Ade and C. J. Brabec, *J. Mater. Chem. A*, 2017, **5**, 18101–18110.
6 C. W. Tang, *Appl. Phys. Lett.*, 1986, **48**, 183–185.
7 G. J. Hedley, A. Ruseckas and I. D. Samuel, *Chem. Rev.*, 2017, **117**, 796–837.
8 B. Siegmund, M. T. Sajjad, J. Widmer, D. Ray, C. Koerner, M. Riede, K. Leo, I. D. Samuel and K. Vandewal, *Adv. Mater.*, 2017, **29**, 1604424.
9 G. Yu, J. Gao, J. C. Hummelen, F. Wudl and A. J. Heeger, *Science*, 1995, **270**, 1789–1791.
10 G. Zhang, J. Zhao, P. C. Y. Chow, K. Jiang, J. Zhang, Z. Zhu, J. Zhang, F. Huang and H. Yan, *Chem. Rev.*, 2018, **118**, 3447–3507.
11 W. Huang, P. Cheng, Y. M. Yang, G. Li and Y. Yang, *Adv. Mater.*, 2018, **30**, 1705706.
12 S. Zhang, L. Ye and J. Hou, *Adv. Energy Mater.*, 2016, **6**, 1502529.
13 J. Yuan, Y. Zhang, L. Zhou, G. Zhang, H.-L. Yip, T.-K. Lau, X. Lu, C. Zhu, H. Peng, P. A. Johnson, M. Leclerc, Y. Cao, J. Ulanski, Y. Li and Y. Zou, *Joule*, 2019, **3**, 1140–1151.
14 X. Xu, K. Feng, Z. Bi, W. Ma, G. Zhang and Q. Peng, *Adv. Mater.*, 2019, e1901872.
15 B. Fan, D. Zhang, M. Li, W. Zhong, Z. Zeng, L. Ying, F. Huang and Y. Cao, *Sci. Chi. Chem.*, 2019, **62**, 746–752.
16 A. Tang, W. Song, B. Xiao, J. Guo, J. Min, Z. Ge, J. Zhang, Z. Wei and E. Zhou, *Chem. Mater.*, 2019, **31**, 3941–3947.
17 A. Tang, B. Xiao, Y. Wang, F. Gao, K. Tajima, H. Bin, Z.-G. Zhang, Y. Li, Z. Wei and E. Zhou, *Adv. Funct. Mater.*, 2018, **28**, 1704507.
18 A. Tang, B. Xiao, F. Chen, J. Zhang, Z. Wei and E. Zhou, *Adv. Energy Mater.*, 2018, **8**, 1801582.
19 J. Chen, Z. Bi, X. Xu, Q. Zhang, S. Yang, S. Guo, H. Yan, W. You and W. Ma, *Adv. Sci.*, 2019, 1801560.
20 L. Ye, B. A. Collins, X. Jiao, J. Zhao, H. Yan and H. Ade, *Adv. Energy Mater.*, 2018, **8**, 1703058.
21 H. Lee, C. Park, D. H. Sin, J. H. Park and K. Cho, *Adv. Mater.*, 2018, e1800453.
22 L. Huang, G. Wang, W. Zhou, B. Fu, X. Cheng, L. Zhang, Z. Yuan, S. Xiong, L. Zhang, Y. Xie, A. Zhang, Y. Zhang, W. Ma, W. Li, Y. Zhou, E. Reichmanis and Y. Chen, *ACS Nano*, 2018, **12**, 4440–4452.
23 N. Li, J. D. Perea, T. Kassar, M. Richter, T. Heumueller, G. J. Matt, Y. Hou, N. S. Guldal, H. Chen, S. Chen, S. Langner, M. Berlinghof, T. Unruh and C. J. Brabec, *Nat. Commun.*, 2017, **8**, 14541.
24 H. Zhang, R. C. Shallcross, N. Li, T. Stubhan, Y. Hou, W. Chen, T. Ameri, M. Turbiez, N. R. Armstrong and C. J. Brabec, *Adv. Energy Mater.*, 2016, **6**, 1502195.
25 Y. Zhang, Y. Xu, M. J. Ford, F. Li, J. Sun, X. Ling, Y. Wang, J. Gu, J. Yuan and W. Ma, *Adv. Energy Mater.*, 2018, **8**, 1800029.
26 X. Yang, M. Niu, P. Bi, Z. Chen, J. Liu and X. Hao, *J. Phys. Chem. C*, 2018, **122**, 9843–9851.
27 R. Yu, H. Yao, L. Hong, Y. Qin, J. Zhu, Y. Cui, S. Li and J. Hou, *Nat. Commun.*, 2018, **9**, 4645.
28 P. Cheng, C. Yan, T. K. Lau, J. Mai, X. Lu and X. Zhan, *Adv. Mater.*, 2016, **28**, 5822–5829.
29 Y. Xu, X. Huang, J. Yuan and W. Ma, *ACS Appl. Mater. Interfaces*, 2018, **10**, 24037–24045.
30 P. Cheng, C. Yan, Y. Wu, J. Wang, M. Qin, Q. An, J. Cao, L. Huo, F. Zhang, L. Ding, Y. Sun, W. Ma and X. Zhan, *Adv. Mater.*, 2016, **28**, 8021–8028.
31 Z. Li, F. Wu, H. Lv, D. Yang, Z. Chen, X. Zhao and X. Yang, *Adv. Mater.*, 2015, **27**, 6999–7003.
32 X. Du, T. Heumueller, W. Gruber, A. Classen, T. Unruh, N. Li and C. J. Brabec, *Joule*, 2018, **3**, 215–226.
33 H. Cha, J. Wu, A. Wadsworth, J. Nagitta, S. Limbu, S. Pont, Z. Li, J. Searle, M. F. Wyatt, D. Baran, J. S. Kim, I. McCulloch and J. R. Durrant, *Adv. Mater.*, 2017, **29**, 1701156.
34 Y. Wang and X. Zhan, *Adv. Energy Mater.*, 2016, **6**, 1600414.
35 Y. Cui, S. Zhang, N. Liang, J. Kong, C. Yang, H. Yao, L. Ma and J. Hou, *Adv. Mater.*, 2018, e1802499.
36 R. Sun, J. Guo, C. Sun, T. Wang, Z. Luo, Z. Zhang, X. Jiao, W. Tang, C. Yang, Y. Li and J. Min, *Energy Environ. Sci.*, 2019, **12**, 384–395.
37 O. Wiedenmann, A. Abdellah, G. Scarpa and P. Lugli, *J. Phys.: Conf. Ser.*, 2009, **193**, 012115.
38 R. R. Lunt, N. C. Giebink, A. A. Belak, J. B. Benziger and S. R. Forrest, *J. Appl. Phys.*, 2009, **105**, 053711.
39 J.-H. Huang, Z.-Y. Ho, T.-H. Kuo, D. Kekuda, C.-W. Chu and K.-C. Ho, *J. Mater. Chem.*, 2009, **19**, 4077.
40 A. L. Ayzner, C. J. Tassone, S. H. Tolbert and B. J. Schwartz, *J. Phys. Chem. C*, 2009, **113**, 20050–20060.
41 H. Li, Z. Qi and J. Wang, *Appl. Phys. Lett.*, 2013, **102**, 213901.
42 Y. Lin, L. Ma, Y. Li, Y. Liu, D. Zhu and X. Zhan, *Adv. Energy Mater.*, 2013, **3**, 1166–1170.

43 S. Dong, K. Zhang, B. Xie, J. Xiao, H.-L. Yip, H. Yan, F. Huang and Y. Cao, *Adv. Energy Mater.*, 2019, **9**, 1802832.
44 J. Min, Y. N. Luponosov, C. Cui, B. Kan, H. Chen, X. Wan, Y. Chen, S. A. Ponomarenko, Y. Li and C. J. Brabec, *Adv. Energy Mater.*, 2017, **7**, 1700465.
45 H. Bin, L. Gao, Z. G. Zhang, Y. Yang, Y. Zhang, C. Zhang, S. Chen, L. Xue, C. Yang, M. Xiao and Y. Li, *Nat. Commun.*, 2016, **7**, 13651.
46 Z. Zhang, J. Yu, X. Yin, Z. Hu, Y. Jiang, J. Sun, J. Zhou, F. Zhang, T. P. Russell, F. Liu and W. Tang, *Adv. Funct. Mater.*, 2018, **28**, 1705095.
47 J. Luke, E. M. Speller, A. Wadsworth, M. F. Wyatt, S. Dimitrov, H. K. H. Lee, Z. Li, W. C. Tsoi, I. McCulloch, D. Bagnis, J. R. Durrant and J. S. Kim, *Adv. Energy Mater.*, 2019, **9**, 1803755.
48 J. Min, Y. N. Luponosov, N. Gasparini, M. Richter, A. V. Bakirov, M. A. Shcherbina, S. N. Chvalun, L. Grodd, S. Grigorian, T. Ameri, S. A. Ponomarenko and C. J. Brabec, *Adv. Energy Mater.*, 2015, **5**, 1500386.
49 J. Min, C. Bronnbauer, Z.-G. Zhang, C. Cui, Y. N. Luponosov, I. Ata, P. Schweizer, T. Przybilla, F. Guo, T. Ameri, K. Forberich, E. Spiecker, P. Bäuerle, S. A. Ponomarenko, Y. Li and C. J. Brabec, *Adv. Funct. Mater.*, 2016, **26**, 4543–4550.
50 Q. Liu, J. Toudert, T. Li, M. Kramarenko, G. Martínez-Denegri, L. Ciammaruchi, X. Zhan and J. Martorell, *Adv. Energy Mater.*, 2019, 1900463.
51 G. Zhang, R. Xia, Z. Chen, J. Xiao, X. Zhao, S. Liu, H.-L. Yip and Y. Cao, *Adv. Energy Mater.*, 2018, **8**, 1801609.
52 Y. N. Luponosov, J. Min, D. A. Khanin, D. Baran, S. A. Pisarev, S. M. Peregudova, P. V. Dmitryakov, S. N. Chvalun, G. V. Cherkaev, E. A. Svidchenko, T. Ameri, C. J. Brabec and S. A. Ponomarenko, *J. Photon. Energy*, 2015, **5**, 057213.
53 N. Gasparini, S. Kahmann, M. Salvador, J. D. Perea, A. Sperlich, A. Baumann, N. Li, S. Rechberger, E. Spiecker, V. Dyakonov, G. Portable, M. A. Loi, C. J. Brabec and T. Ameri, *Adv. Energy Mater.*, 2019, **9**, 1803394.
54 S. Chandrabose, K. Chen, A. J. Barker, J. J. Sutton, S. K. K. Prasad, J. Zhu, J. Zhou, K. C. Gordon, Z. Xie, X. Zhan and J. M. Hodgkiss, *J. Am. Chem. Soc.*, 2019, **141**, 6922–6929.
55 A. S. a. Y. Engelborghs, *Photochem. Photobiol.*, 1998, **67**, 475–486.
56 H. Cha, S. Wheeler, S. Holliday, S. D. Dimitrov, A. Wadsworth, H. H. Lee, D. Baran, I. McCulloch and J. R. Durrant, *Adv. Funct. Mater.*, 2018, **28**, 1704389.
57 T. Wang, R. Sun, S. Xu, J. Guo, W. Wang, J. Guo, X. Jiao, J. Wang, S. Jia, X. Zhu, Y. Li and J. Min, *J. Mater. Chem. A*, 2019, **7**, 14070–14078.
58 N. Gasparini, X. Jiao, T. Heumueller, D. Baran, G. J. Matt, S. Fladischer, E. Spiecker, H. Ade, C. J. Brabec and T. Ameri, *Nat. Energy*, 2016, **1**, 16118.
59 L. Ye, Y. Xiong, Q. Zhang, S. Li, C. Wang, Z. Jiang, J. Hou, W. You and H. Ade, *Adv. Mater.*, 2018, **30**, 1705485.
60 Z. Li, Y. Lei, P. Zhu, W. Zhong, N. Li, F. Liu, F. Huang and Y. Cao, *Energy Environ. Sci.*, 2019, **12**, 157–163.
61 Y. Yan, X. Liu and T. Wang, *Adv. Mater.*, 2017, **29**, 1601674.
62 J. Guo, H. Bin, W. Wang, B. Chen, J. Guo, R. Sun, Z.-G. Zhang, X. Jiao, Y. Li and J. Min, *J. Mater. Chem. A*, 2018, **6**, 15675–15683.
63 R. Yu, H. Yao, Z. Chen, J. Xin, L. Hong, Y. Xu, Y. Zu, W. Ma and J. Hou, *Adv. Mater.*, 2019, 01900477.
64 J. Li, Y. Wang, Z. Liang, N. Wang, J. Tong, C. Yang, X. Bao and Y. Xia, *ACS Appl. Mater. Interfaces*, 2019, **11**, 7022–7029.
65 J. Min, X. Jiao, I. Ata, A. Osvet, T. Ameri, P. Bäuerle, H. Ade and C. J. Brabec, *Adv. Energy Mater.*, 2016, **6**, 1502579.
66 N. Gasparini, A. Wadsworth, M. Moser, D. Baran, I. McCulloch and C. J. Brabec, *Adv. Energy Mater.*, 2018, **8**, 1703298.
67 R. Sun, D. Deng, J. Guo, Q. Wu, J. Guo, M. Shi, K. Shi, T. Wang, L. Xue, Z. Wei and J. Min, *Energy Environ. Sci.*, 2019, **12**, 2518–2528.
68 B. Xiao, M. Zhang, J. Yan, G. Luo, K. Gao, J. Liu, Q. You, H.-B. Wang, C. Gao, B. Zhao, X. Zhao, H. Wu and F. Liu, *Nano Energy*, 2017, **39**, 478–488.
69 N. K. Elumalai and A. Uddin, *Energy Environ. Sci.*, 2016, **9**, 391–410.
70 Y. Xie, T. Li, J. Guo, P. Bi, X. Xue, H. S. Ryu, Y. Cai, J. Min, L. Huo, X. Hao, H. Y. Woo, X. Zhan and Y. Sun, *ACS Energy Lett.*, 2019, **4**, 1196–1203.
71 J. Yao, T. Kirchartz, M. S. Vezie, M. A. Faist, W. Gong, Z. He, H. Wu, J. Troughton, T. Watson, D. Bryant and J. Nelson, *Phys. Rev. Appl.*, 2015, **4**, 2331–7019.
72 T. Heumueller, W. R. Mateker, A. Distler, U. F. Fritze, R. Cheacharoen, W. H. Nguyen, M. Biele, M. Salvador, M. von Delius, H.-J. Egelhaaf, M. D. McGehee and C. J. Brabec, *Energy Environ. Sci.*, 2016, **9**, 247–256.
73 W. Wang, B. Chen, X. Jiao, J. Guo, R. Sun, J. Guo and J. Min, *Org. Electron.*, 2019, **70**, 78–85.

